



Construction of perovskite homojunction for highly efficient perovskite solar cells by SCAPS-1D

Jiexiang Liang, Yanan Wang, Yufeng Zhang*, Xiaolin Liu*, Jia Lin*

Department of Physics, Shanghai University of Electric Power, Shanghai 200090, China



ARTICLE INFO

Keywords:

Carrier recombination
MAPbI₃(p)/MAPbI₃(n) homojunction
Doping concentration
Thickness

ABSTRACT

Perovskite solar cells (PSCs) have been widely studied due to their outstanding photovoltaic (PV) performance. However, carrier recombination in perovskite is one of the main factors limiting their PV performance. Here, by constructing a p-type MAPbI₃/n-type MAPbI₃ (MAPbI₃(p)/MAPbI₃(n)) homojunction using SCAPS-1D, an electric field was created inside the homojunction to reduce the recombination of photogenerated carriers, and the power conversion efficiency (PCE) increased from 13.82 % to 19.14 %. Besides, the effects of the doping concentration of MAPbI₃(n) and MAPbI₃(p) on PV performance were explored. A PCE of 19.98 % was reached at the optimal doping concentration. Finally, the influences of the thickness of MAPbI₃(n) and MAPbI₃(p) on the PV performance were investigated, and a PCE of 22.00 % was achieved when the thickness of MAPbI₃(n) and MAPbI₃(p) were 0.45 and 2.25 μm, respectively. This work provides a strategy for constructing perovskite homojunction for highly efficient PSCs.

1. Introduction

Over the years, the power conversion efficiency (PCE) of perovskite solar cells (PSCs) has increased from 3.8 % [1] to over 26 % [2] due to the development of technologies including the engineering of passivators [3–8], solvents [9,10], components [11–17], energy bands [18–20], and dimensions [21–23]. Through these techniques, recombination of photogenerated charge carriers is suppressed in diverse ways, which is beneficial to enhance their photovoltaic (PV) performances. Since the separation of electron-hole pairs and the transportation of charge carriers rely on the built-in electric field (BEF) inside the space charge region (SCR) between the functional layers in the PSCs, the optimization of the distribution of BEF in the devices is crucial to enhancing the PCE of the PSCs. Although a BEF exists between the perovskite and the charge transport layers, there is still a high total recombination rate inside the perovskite light-absorbing layer because of the lack of an SCR inside the perovskite. From the above discussions, the formation of a large-width SCR inside the perovskite is crucial for further reduction of total recombination.

The creation of a perovskite homojunction can generate BEF by the formation of an SCR of a certain width in the light-absorbing layer, which further promotes charge carrier separation and directional transport, thus reducing the total recombination. Li et al. prepared a

perovskite homojunction by controlling the stoichiometric ratios of precursors, and the PCE was enhanced from 17.76 % to 20.80 % [24]. Wu et al. treated the surface of perovskite with InBr₃ to make the top of perovskite more n-type, which allowed the formation of a homojunction between the surface and the interior of perovskite, improving the BEF and promoting the separation of charge carriers. As a result, a PCE of 22.2 % was achieved [25]. These experimental results have demonstrated that the introduction of homojunction can enhance the PCE of PSCs, but the underlying mechanism of the role of perovskite homojunction on the PV performances was not fully understood, and the effects of the doping concentration and thickness of the perovskite layer on the PV performance have not been systematically explored.

In this study, we constructed the MAPbI₃(p)/MAPbI₃(n) homojunction using SCAPS-1D [26]. This software is widely used to simulate the PV performance of solar cells [27–30]. By creating an SCR in the MAPbI₃(p)/MAPbI₃(n) homojunction, the PCE of the PSC was raised from 13.82 % to 19.14 %. In addition, the impacts of donor doping concentration (N_D) of MAPbI₃(n) and acceptor doping concentration (N_A) of MAPbI₃(p) on the PV performance of PSCs were studied. A PCE of 19.98 % was reached when the N_D of MAPbI₃(n) was $1 \times 10^{17} \text{ cm}^{-3}$ and the N_A of MAPbI₃(p) was $1 \times 10^{18} \text{ cm}^{-3}$. Furthermore, the influences of the thickness of MAPbI₃(n) and MAPbI₃(p) on the PV performance were explored, and a PCE of 22.00 % was achieved when the

* Corresponding authors.

E-mail addresses: 2009000018@shiep.edu.cn (Y. Zhang), xliu@shiep.edu.cn (X. Liu), jlin@shiep.edu.cn (J. Lin).

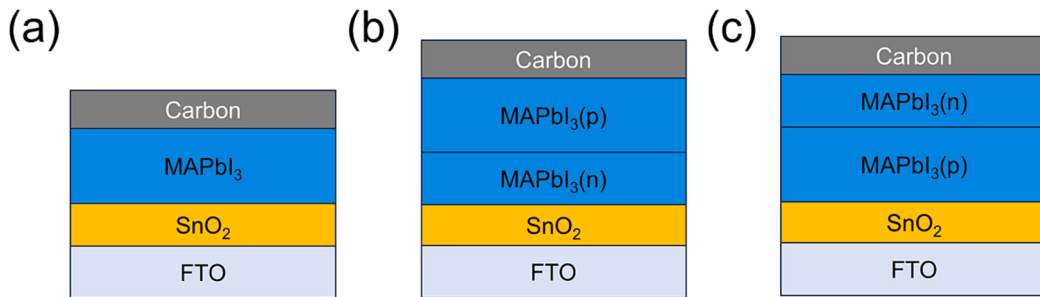


Fig. 1. Schematic diagram of the structures of (a) control device, and the devices containing (b) the MAPbI₃(p)/MAPbI₃(n) homojunction, and (c) the MAPbI₃(n)/MAPbI₃(p) homojunction.

Table 1
Initial physical parameters of each functional layer of the PSCs.

Parameters	FTO	SnO ₂	MAPbI ₃	MAPbI ₃ (p)	MAPbI ₃ (n)
Thickness (nm)	400	30	500	250	250
Bandgap (eV)	3.500	3.300	1.550	1.550	1.550
Electron affinity (eV)	4.000	4.000	3.930	3.930	3.930
Dielectric permittivity (relative)	9.000	9.000	6.500	6.500	6.500
Conduction band effective density of states (cm ⁻³)	2.2 × 10 ¹⁸	2.2 × 10 ¹⁷	1.0 × 10 ¹⁹	1.0 × 10 ¹⁹	1.0 × 10 ¹⁹
Valence band effective density of states (cm ⁻³)	1.8 × 10 ¹⁸	2.2 × 10 ¹⁶	1.0 × 10 ¹⁷	1.0 × 10 ¹⁷	1.0 × 10 ¹⁷
Electron mobility (cm ² /Vs)	20	200	50	50	50
Hole mobility (cm ² /Vs)	10	80	50	50	50
N _D (cm ⁻³)	1.0 × 10 ¹⁹	1.0 × 10 ¹⁷	0	0	1.0 × 10 ¹⁷
N _A (cm ⁻³)	0	0	1.0 × 10 ¹⁷	1.0 × 10 ¹⁷	0
Defect density (cm ⁻³)	1.0 × 10 ¹⁴	1.0 × 10 ¹⁵	1.0 × 10 ¹⁶	1.0 × 10 ¹⁶	1.0 × 10 ¹⁶

thicknesses of MAPbI₃(n) and MAPbI₃(p) were 0.45 and 2.25 μm, respectively.

2. Device structure and simulation parameters

In this study, a temperature of 300 K and standard AM 1.5G illumination were applied throughout the study. The structures of the PSCs used for simulation are carbon/MAPbI₃/SnO₂/FTO, carbon/MAPbI₃(p)/MAPbI₃(n)/SnO₂/FTO, and carbon/MAPbI₃(n)/MAPbI₃(p)/SnO₂/FTO, as shown in Fig. 1. The N_A of MAPbI₃ was set to be $1.0 \times 10^{17} \text{ cm}^{-3}$ and

Table 2
PV parameters of PSCs with different device configurations.

Device configuration	V _{OC} (V)	J _{SC} (mA/cm ²)	FF (%)	PCE (%)
carbon/MAPbI ₃ /SnO ₂ /FTO	1.00	18.47	74.77	13.82
carbon/MAPbI ₃ (n)/MAPbI ₃ (p)/SnO ₂ /FTO	0.58	12.38	65.54	4.75
carbon/MAPbI ₃ (p)/MAPbI ₃ (n)/SnO ₂ /FTO	1.05	21.55	84.58	19.14

the thickness of MAPbI₃ was set to be 500 nm. Meanwhile, the defect density (N_d) of MAPbI₃ was set to be $1.0 \times 10^{16} \text{ cm}^{-3}$. Since the ratio of radiative and Auger recombination in the total recombination of carriers will gradually increase as the carrier concentration increases, radiative and Auger recombination of carriers were also taken into account in this study, and the radiative and Auger recombination coefficients of MAPbI₃ were set to be $8.1 \times 10^{-11} \text{ cm}^3 \text{ s}^{-1}$ and $1.1 \times 10^{-28} \text{ cm}^6 \text{ s}^{-1}$, respectively [31]. In addition to this, interfacial defect layers (IDLs) were set on the upper surface of MAPbI₃(p) and the lower surface of MAPbI₃(n), respectively, and the thicknesses of both IDLs were set to be 10 nm, and their N_t were set to be $4.0 \times 10^{17} \text{ cm}^{-3}$. Other initial parameters are shown in Table 1 [32,33].

3. Results and discussion

3.1. Influences of perovskite homojunction on the PV performance of PSCs

The current density–voltage (J-V) curves for the control device, and the devices containing the MAPbI₃(p)/MAPbI₃(n) homojunction and the MAPbI₃(n)/MAPbI₃(p) homojunction are shown in Fig. 2(a). The PV parameters including the open-circuit voltage (V_{OC}), short-circuit

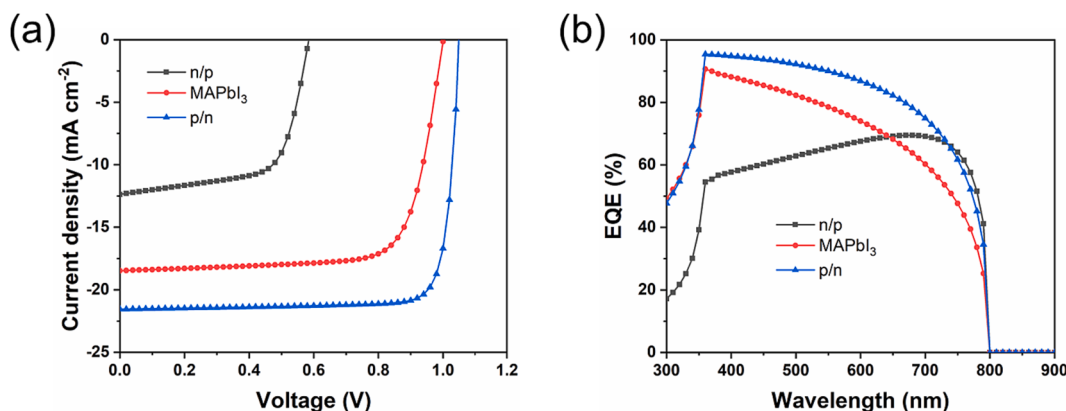


Fig. 2. (a) J-V curves, (b) EQE curves of the control device, and the devices containing the MAPbI₃(p)/MAPbI₃(n) homojunction and MAPbI₃(n)/MAPbI₃(p) homojunction. MAPbI₃(p) and MAPbI₃(n) are abbreviated as p and n.

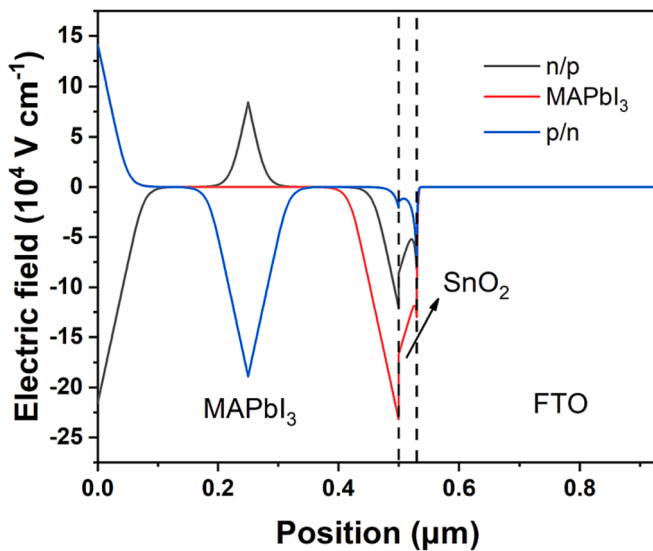


Fig. 3. Electric field of the control device, and the devices containing the MAPbI₃(p)/MAPbI₃(n) homojunction and MAPbI₃(n)/MAPbI₃(p) homojunction. MAPbI₃(p) and MAPbI₃(n) are abbreviated as p and n.

current density (J_{SC}), fill factor (FF), and PCE for these three PSCs are presented in Table 2. The PSC with the carbon/MAPbI₃/SnO₂/FTO structure has a PCE of 13.82 %. The J_{SC} of the device containing the MAPbI₃(p)/MAPbI₃(n) homojunction was improved from 18.47 to 21.55 mA/cm², resulting in a PCE increase from 13.82 % to 19.14 %. However, the PV performance of the device containing the MAPbI₃(n)/MAPbI₃(p) homojunction decreased significantly, and its PCE dropped

from 13.82 % to 4.75 %. The external quantum efficiency (EQE) curves show a similar conclusion, as shown in Fig. 2(b).

Fig. 3 shows the electric field distribution at different locations in the PSC. Fig. 4 exhibits the recombination strength of the different carrier recombination paths for these three structures. It can be found that the total recombination rate is mainly determined by the SRH recombination, and the recombination strength corresponding to the other recombination paths are negligible with respect to the SRH recombination. The changes in the PV parameters of PSCs with different device configurations are because the introduction of homojunction induces a change in the electric field due to the formation of an SCR inside the perovskite, which affects the separation and transportation of photo-generated charge carriers. Since no homojunction is formed inside the control device, no additional electric field is formed (Figs. 3 and 5(a)). For the device containing the MAPbI₃(p)/MAPbI₃(n) homojunction, a BEF pointing from the MAPbI₃(n) region to the MAPbI₃(p) region is formed inside the perovskite layer (Figs. 3 and 5(b)). Such a BEF promotes the charge carrier separation and drives the photogenerated electrons toward SnO₂ as well as holes toward the carbon electrode, which inhibits SRH, radiative, and Auger recombinations. However, for the device containing the MAPbI₃(n)/MAPbI₃(p) homojunction, the BEF is in the opposite direction to that inside the MAPbI₃(p)/MAPbI₃(n) homojunction, as shown in Fig. 5(c). This BEF prevents the photo-generated electrons from moving toward SnO₂ and the holes from moving toward the carbon electrode, leading to severe recombination paths inside the perovskite layer.

3.2. Doping of MAPbI₃

The distribution and strength of the BEF in the light-absorbing layer can be controlled by altering doping concentration. In the experiment, doping type and doping concentration of MAPbI₃ can be modulated by

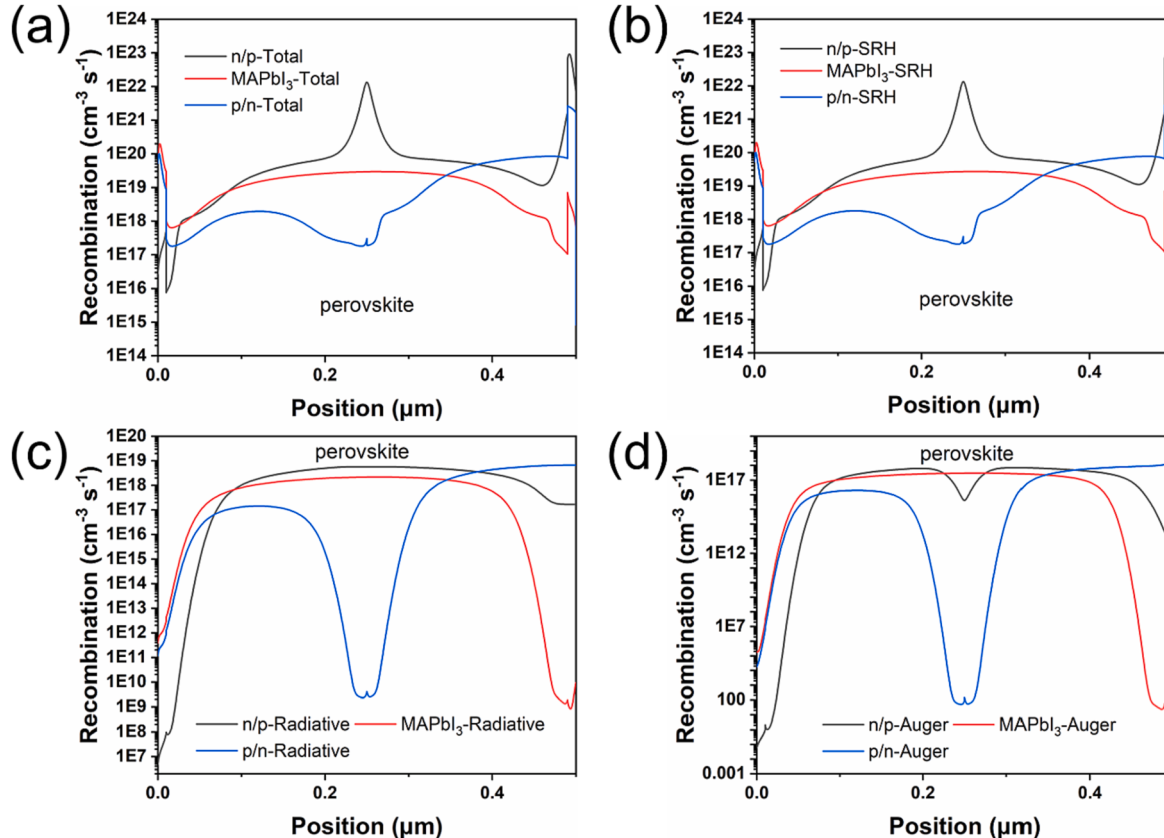


Fig. 4. (a) Total, (b) SRH, (c) Radiative and (d) Auger recombination rates of the control device, and the devices containing the MAPbI₃(p)/MAPbI₃(n) homojunction and MAPbI₃(n)/MAPbI₃(p) homojunction. MAPbI₃(p) and MAPbI₃(n) are abbreviated as p and n in the figure.

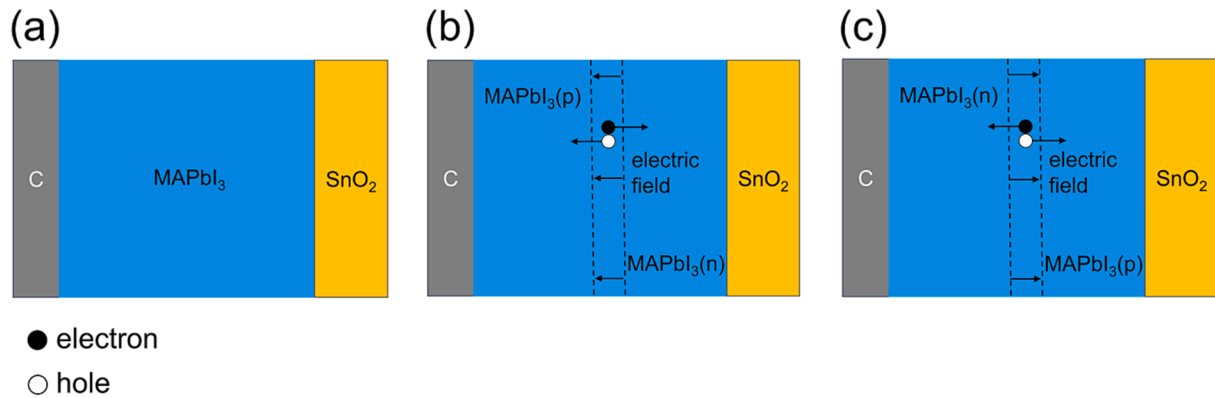


Fig. 5. Schematic diagram of the electric field distribution inside the perovskite layer of (a) the control device, and the devices containing the (b) MAPbI₃(p)/MAPbI₃(n) homojunction and (c) MAPbI₃(n)/MAPbI₃(p) homojunction.

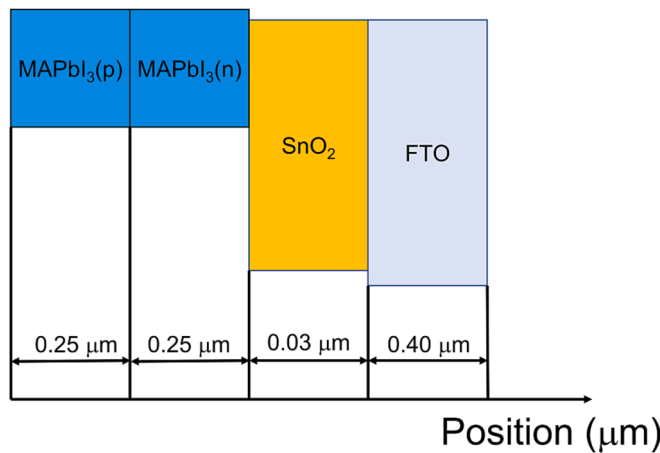


Fig. 6. Distribution of various functional layers in the PSC.

changing the molar ratio of PbI₂/MAI, annealing processes, and heterovalent ion doping [34].

3.3. Device optimization

3.3.1. Optimization of N_D of MAPbI₃(n)

In this section, we set the N_D of MAPbI₃(n) in the range of 1×10^{15} to $1 \times 10^{19} \text{ cm}^{-3}$, and fixed the N_A of MAPbI₃(p) to be $1 \times 10^{17} \text{ cm}^{-3}$. The positional distribution of each functional layer of the PSC device is shown in Fig. 6.

The J-V curves at different N_D values of MAPbI₃(n) are shown in

Table 3
PV parameters of devices corresponding to different N_D values.

N _D of MAPbI ₃ (n) (cm^{-3})	V _{OC} (V)	J _{SC} (mA/cm^2)	FF (%)	PCE (%)
1×10^{15}	1.05	21.56	81.00	18.27
1×10^{16}	1.05	21.66	82.53	18.77
1×10^{17}	1.05	21.55	84.58	19.14
1×10^{18}	1.05	20.61	84.97	18.34
1×10^{19}	1.04	9.46	82.61	8.15

Fig. 7(a), and the corresponding PV parameters are summarized in Table 3. It can be noticed that with the increase of N_D in MAPbI₃(n), the V_{OC} remained almost unchanged, while J_{SC} increases and then decreases and reaches its maximum value when N_D is $1 \times 10^{16} \text{ cm}^{-3}$. This is consistent with the EQE curves in Fig. 7(b). Similar to the trend of J_{SC}, FF and PCE reached their maximum values when N_D was $1 \times 10^{18} \text{ cm}^{-3}$ and $1 \times 10^{17} \text{ cm}^{-3}$, respectively. The largest PCE value reached 19.14 %.

We calculated the electric field inside the homojunction by the following equations:

$$E(x) = \frac{-eN_D}{\epsilon_s}(x_n - x) \quad (0 \leq x \leq x_n) \quad (1)$$

$$x_n = \sqrt{\frac{2\epsilon_s V_{bi}}{e} \left(\frac{N_A}{N_D} \right) \left(\frac{1}{N_A + N_D} \right)} \quad (2)$$

$$E(x) = \frac{-eN_A}{\epsilon_s}(x_p + x) \quad (-x_p \leq x \leq 0) \quad (3)$$

$$x_p = \sqrt{\frac{2\epsilon_s V_{bi}}{e} \left(\frac{N_D}{N_A} \right) \left(\frac{1}{N_A + N_D} \right)} \quad (4)$$

where ϵ_s is the dielectric constant of MAPbI₃(n), e is elementary charge,

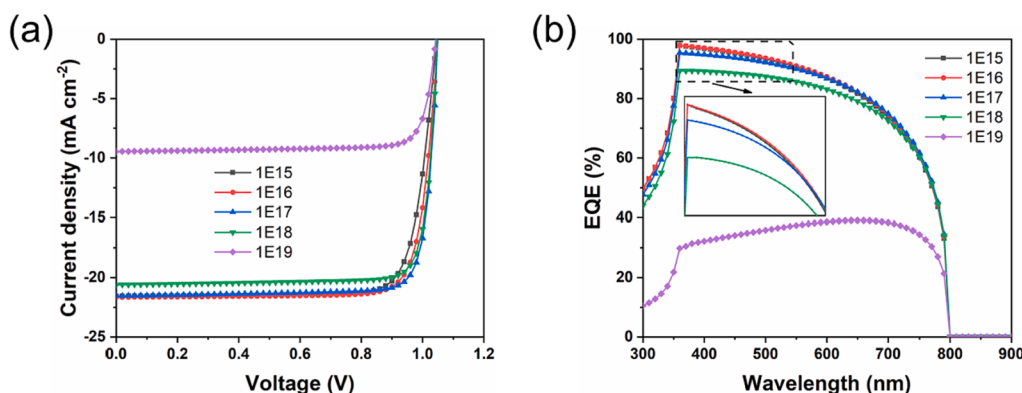


Fig. 7. (a) J-V curves, and (b) EQE curves of devices corresponding to different N_D values.

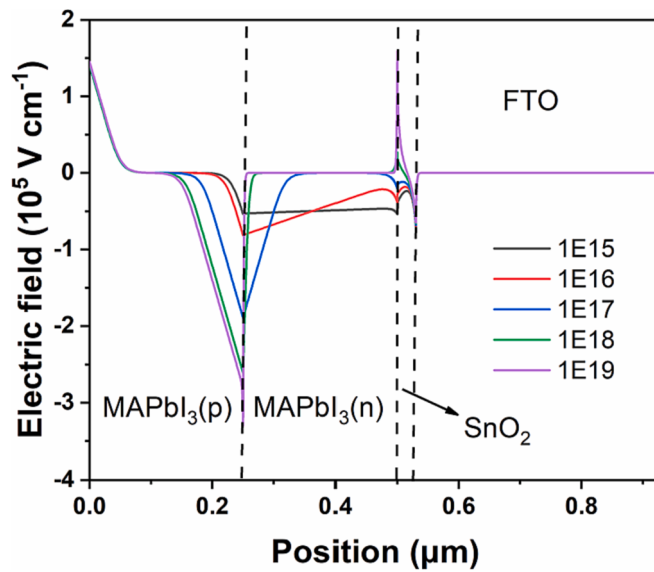


Fig. 8. Electric field of devices corresponding to different N_D values.

V_{bi} is the built-in potential difference, and x_n and x_p are the widths of the SCR in $\text{MAPbI}_3(\text{n})$ and $\text{MAPbI}_3(\text{p})$, respectively. Equation (1) treats the position corresponding to the maximum of the BEF as zero. We can find that with the increase of N_D in $\text{MAPbI}_3(\text{n})$, the maximum values of the BEF between $\text{MAPbI}_3(\text{n})$ and $\text{MAPbI}_3(\text{p})$ gradually increase, while the widths of the SCR in $\text{MAPbI}_3(\text{n})$ decreases gradually but SCR in $\text{MAPbI}_3(\text{p})$ increases gradually, as shown in Fig. 8, which affect the transport of photogenerated charge carriers. The results of the effects of the variation of the BEF on carriers transport can be obtained from Fig. 9. Fig. 9 exhibits the recombination strength of different recombination paths of PSCs at different N_D values of $\text{MAPbI}_3(\text{n})$. From Fig. 9(a), it can

be found that the total recombination in the region near the right side of $\text{MAPbI}_3(\text{n})$ gradually increases with the increase of N_D , however, the total recombination in the region near the right side of $\text{MAPbI}_3(\text{p})$ gradually decreases, which is in agreement with the previously mentioned law of the electric field, respectively. By comparing the relative magnitudes of the total recombination rates on both sides of the interface between $\text{MAPbI}_3(\text{p})$ and $\text{MAPbI}_3(\text{n})$, it can be found that the Total recombination rate in $\text{MAPbI}_3(\text{n})$ plays a dominant role in the J_{SC} , and its pattern is consistent with the variation of the J_{SC} when the values of N_D are in the range of $1 \times 10^{16} \text{ cm}^{-3}$ to $1 \times 10^{19} \text{ cm}^{-3}$. In addition, radiative and Auger recombination have similar patterns of change, as

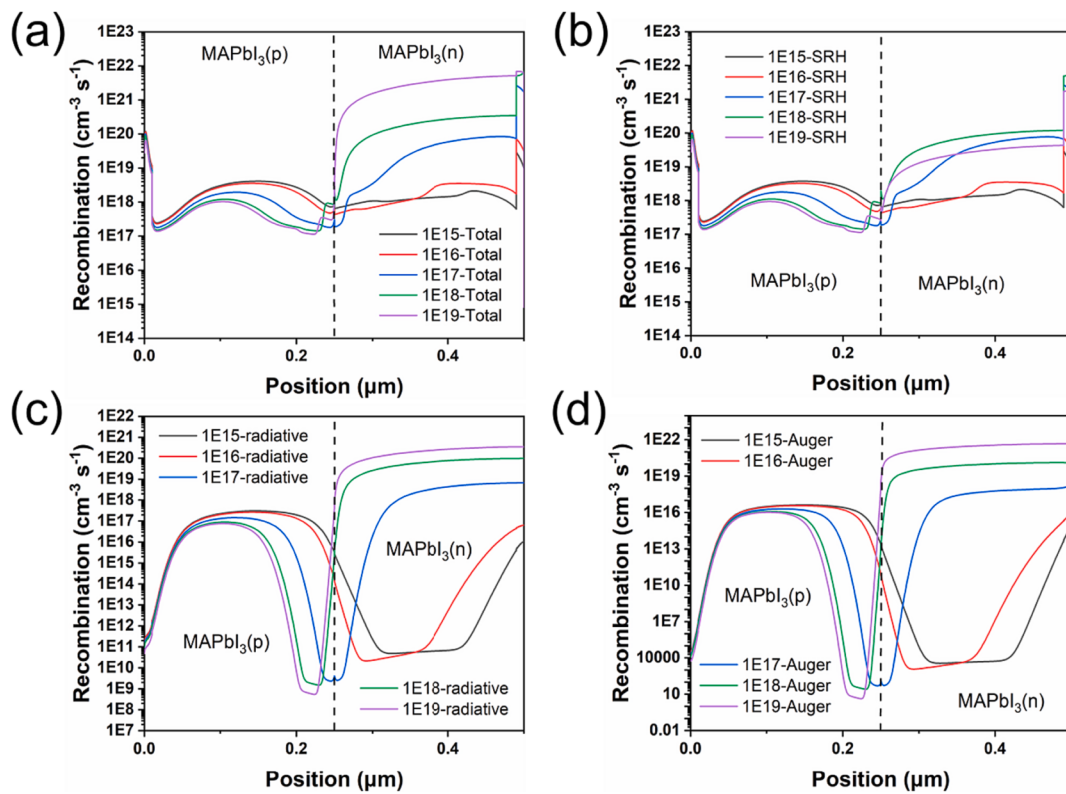


Fig. 9. (a) Total, (b) SRH, (c) radiative and (d) Auger recombination rates of devices corresponding to different N_D values.

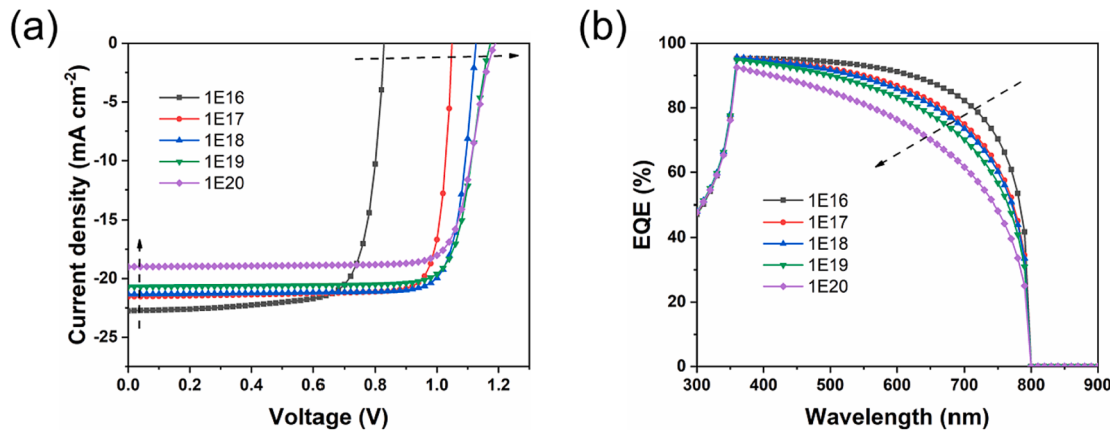


Fig. 10. (a) J-V curves, and (b) EQE curves of the PSCs corresponding to different N_A.

Table 4
PV parameters of devices corresponding to different N_A.

N _A of MAPbI ₃ (p) (cm ⁻³)	V _{OC} (V)	J _{SC} (mA/cm ²)	FF (%)	PCE (%)
1 × 10 ¹⁶	0.83	22.74	76.14	14.36
1 × 10 ¹⁷	1.05	21.55	84.58	19.14
1 × 10 ¹⁸	1.13	21.33	83.09	19.98
1 × 10 ¹⁹	1.17	20.70	80.77	19.61
1 × 10 ²⁰	1.19	18.99	79.75	18.01

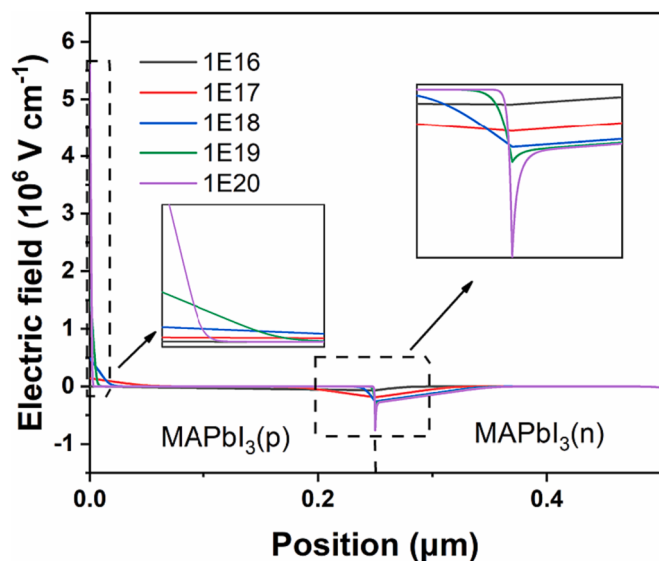


Fig. 11. Electric field of devices corresponding to different N_A values.

shown in Fig. 9(c,d). However, compared with the N_D of 1 × 10¹⁸ cm⁻³, the SRH recombination in the region near the right side of MAPbI₃(n) decreases significantly when the N_D is 1 × 10¹⁹ cm⁻³, as shown in Fig. 9(b). This is because when the N_D is 1 × 10¹⁹ cm⁻³, the concentration of carriers is higher and the paths of carriers recombination are dominated by radiative and Auger recombination.

3.3.2. Optimization of N_A of MAPbI₃(p)

In this section, we set the N_A of MAPbI₃(p) in the range of 1 × 10¹⁶ to 1 × 10²⁰ cm⁻³ and fixed the N_D of MAPbI₃(n) to be 1 × 10¹⁷ cm⁻³. The J-V curves of the PSCs with different N_A values of MAPbI₃(p) are shown in Fig. 10(a), and the corresponding PV parameters are summarized in Table 4. The V_{OC} increases gradually with the increase of N_A of MAPbI₃(p), while J_{SC} decreases with increasing N_A of MAPbI₃(p). FF rises,

falls, and reaches its maximum when N_A equals 1 × 10¹⁷ cm⁻³. It was a maximum value of 19.98 % that PCE reached when N_A was 1 × 10¹⁸ cm⁻³.

The increase in N_A leads to a decrease in I₀ and therefore a corresponding increase in V_{OC}, as demonstrated by the following equations [35]:

$$V_{OC} = \frac{KT}{q} \ln\left(\frac{I_L}{I_0} + 1\right) \quad (5)$$

$$I_0 = q n_i^2 \left(\frac{D_n}{L_n N_A} + \frac{D_p}{L_p N_D} \right) \quad (6)$$

where K is the Boltzmann constant, q represents the magnitude of charge, I_L is the photocurrent, I₀ is the reverse saturation current, D_n and D_p are the electron and hole diffusion coefficient, respectively, L_n and L_p are the electron and hole diffusion lengths, respectively, and n_i² is the product of the electron concentration and the hole concentration at thermal equilibrium. As illustrated in Fig. 11, we can observe that when the N_A in MAPbI₃(p) increases, the maximum values of the BEF between MAPbI₃(n) and MAPbI₃(p) gradually increase. Besides, the widths of the SCR in MAPbI₃(p) gradually decrease while the SCR in MAPbI₃(n) gradually increases. At the same time, as N_A increases, the maximum values of the BEF near the carbon/MAPbI₃(p) interface gradually rise, which prevents the flow of holes to the carbon electrode. This nicely explains the gradual decrease in FF with increasing N_A when N_A is greater than 1 × 10¹⁷ cm⁻³. The effect of the electric field on the separation and transport of photogenerated carriers can also be reflected by the recombination of the carriers, as shown in Fig. 12. It can be found that the Total recombination rate in the region near the middle of MAPbI₃(p) gradually increases with the increase of N_A. Such a pattern is consistent with the changes in J_{SC}. And the pattern of change in the Auger recombination is similar to that of the Total recombination. For SRH recombination, when N_A is greater than 1 × 10¹⁸ cm⁻³, SRH recombination decreases progressively with increasing N_A in most regions of MAPbI₃(p), due to the dominance of Radiative and Auger recombination in this range of N_A. Similarly, when N_A is greater than 1 × 10¹⁹ cm⁻³, Radiative recombination in most regions of MAPbI₃(p)

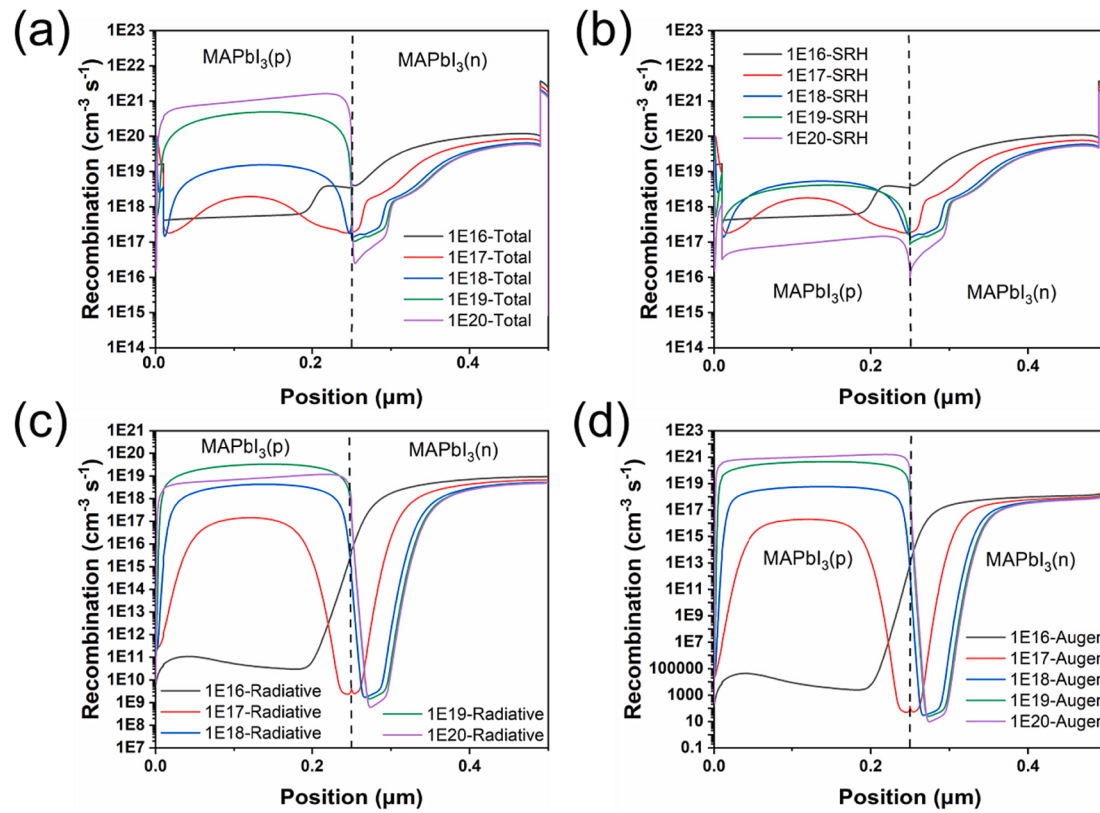


Fig. 12. (a) Total, (b) SRH, (c) radiative and (d) Auger recombination rates of devices corresponding to different N_A values.

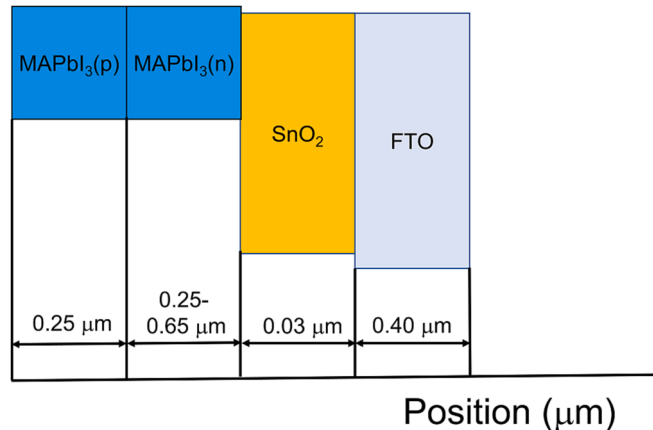


Fig. 13. Distribution of the position of each functional layer of the PSCs with different thickness values of MAPbI₃(n).

gradually decreases with increasing N_A , due to the dominance of Auger recombination when N_A is in this range.

3.3.3. Optimization of MAPbI₃(n) thickness

Since the introduction of homojunction enhances the electric field inside the perovskite, an appropriate increase in the thickness of perovskite layer can further strengthen the PV performance of PSCs. In this section, the thickness of MAPbI₃(n) was varied in the range of 0.25 to 0.65 μm . Meanwhile, the N_D of MAPbI₃(n) was fixed to $1 \times 10^{17} \text{ cm}^{-3}$ and the N_A of MAPbI₃(p) was fixed to $1 \times 10^{18} \text{ cm}^{-3}$ in the study of optimizing the thickness of perovskite.

The location of each functional layer in the PSC is illustrated in Fig. 13. The J-V curves of PSCs with different MAPbI₃(n) thickness values are shown in Fig. 14(a) and the PV parameters are shown in

Table 5. Almost no change in V_{OC} with increasing thickness of MAPbI₃(n). However, when the thickness of MAPbI₃(n) is in the range of 0.25 to 0.45 μm , J_{SC} increases with the increase of thickness, and when the thickness of MAPbI₃(n) is greater than 0.45 μm , J_{SC} decreases with the increase of thickness. At the same time, FF decreases with the increase of thickness. In conclusion, the PCE reached a maximum value of 20.77 % when the thickness of MAPbI₃(n) was 0.45 μm . As the thickness of MAPbI₃(n) increases, the EQE of the device is enhanced for photons with longer wavelengths and weakened for photons with shorter wavelengths, as shown in Fig. 14(b).

Fig. 16 shows the recombination strengths of various carrier recombination paths for PSCs at different MAPbI₃(n) thickness values. It can be found that as the thickness of MAPbI₃(n) increases, the intensities of several recombination paths in the region adjacent to the right side of

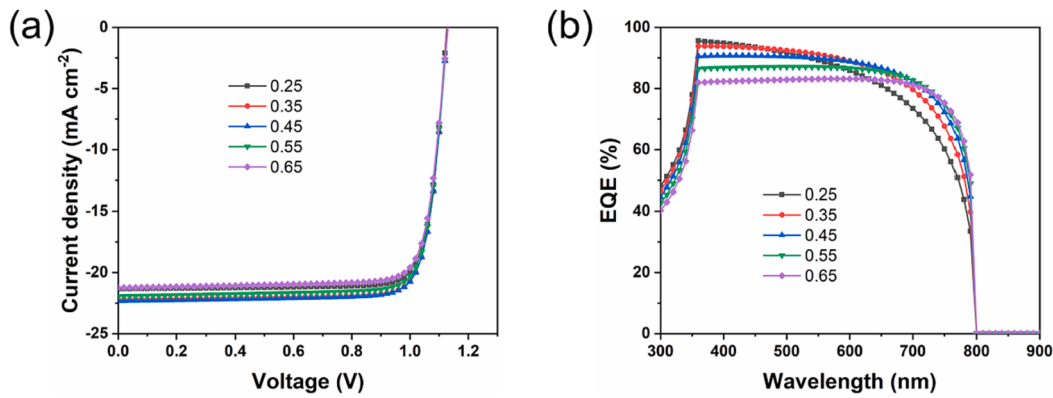


Fig. 14. (a) J-V curves, and (b) EQE curves of the PSCs corresponding to different thickness values of MAPbI₃(n).

Table 5
PV parameters of devices corresponding to different thickness values of MAPbI₃(n).

Thickness of MAPbI ₃ (n) (μm)	V _{OC} (V)	J _{SC} (mA/cm ²)	FF (%)	PCE (%)
0.25	1.13	21.33	83.09	19.98
0.35	1.13	22.20	82.74	20.73
0.45	1.13	22.31	82.40	20.77
0.55	1.13	21.93	82.09	20.35
0.65	1.13	21.24	81.81	19.64

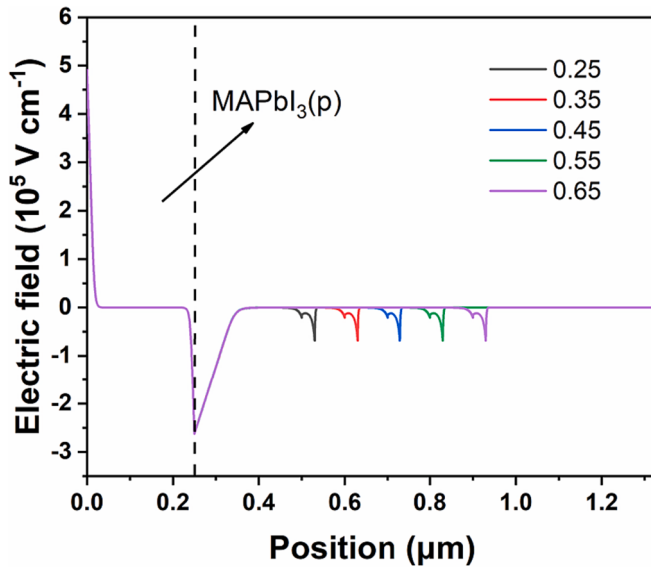


Fig. 15. Electric field of devices corresponding to different thickness values of MAPbI₃(n).

MAPbI₃(n) rise. This is due to the fact that the BEF strengths and the widths of the SCR near the MAPbI₃(p)/MAPbI₃(n) interface remain almost unchanged as the thickness of MAPbI₃(n) changes, as shown in Fig. 15. The increased portion of perovskite layer will be located outside of this SCR, which weakens the charge carrier transport ability. This is also why the FF decreases. At the same time, as the thickness of MAPbI₃(n) increases, it will absorb more photons, and accordingly, MAPbI₃(p) will absorb fewer photons, and thus these four carrier recombination intensities in MAPbI₃(p) will gradually decrease as the thickness of MAPbI₃(n) increases. In conclusion, as the thickness of MAPbI₃(n) increases, more photons will be absorbed by the light-absorbing layer, which contributes to the enhancement of the J_{SC}, but the carrier recombination intensity in MAPbI₃(n) will also increase,

which will lead to the decrease of the J_{SC}, and thus the J_{SC} reaches its maximum value when the thickness of MAPbI₃(n) is 0.45 μm.

3.3.4. Optimization of MAPbI₃(p) thickness

As light can not be fully absorbed by thin MAPbI₃(n) layers, appropriate increase of the thickness of MAPbI₃(p) also increases the absorption of photons. In this section, the thickness of MAPbI₃(p) was set in the range of 0.25 to 2.65 μm. At the same time, the thickness of MAPbI₃(n) was fixed to 0.45 μm.

The location of the different functional layers is shown in Fig. 17. The J-V curves of PSCs with different MAPbI₃(p) thickness values are shown in Fig. 18(a), with specific PV parameters shown in Table 6. It can be noticed that as the thickness of MAPbI₃(p) increases, there is a slight

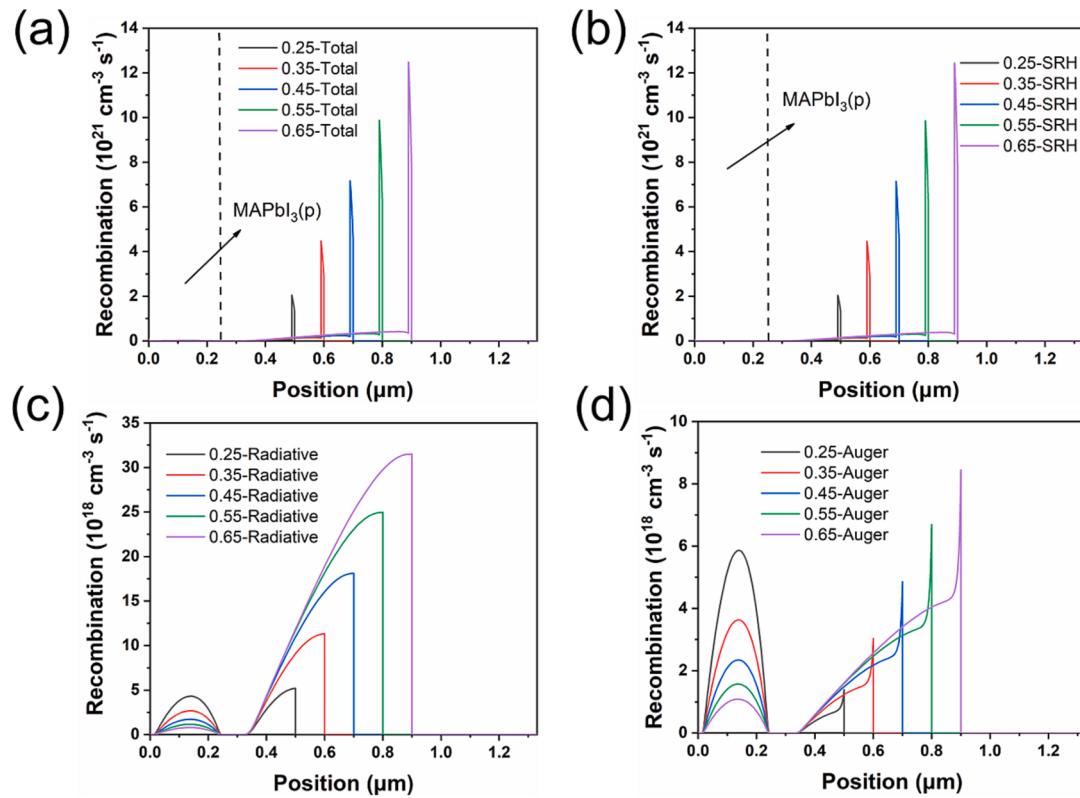


Fig. 16. (a) Total, (b) SRH, (c) radiative and (d) Auger recombination rates of devices corresponding to different thickness values of $\text{MAPbI}_3(\text{n})$.

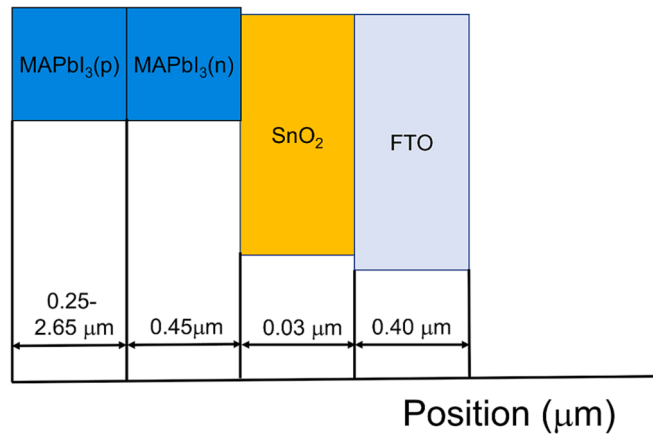


Fig. 17. Distribution of the position of each functional layer of the PSCs with different thickness values of $\text{MAPbI}_3(\text{p})$.

increase in V_{OC} . Meanwhile, as the thickness of $\text{MAPbI}_3(\text{p})$ increases, the J_{SC} and PCE gradually increases and then saturates. However, FF gradually decreases. In a word, to reduce the cost, the thickness of the $\text{MAPbI}_3(\text{p})$ film was determined to be $2.25 \mu\text{m}$, and the PCE reaches a maximum value of 22.00% when the thickness of $\text{MAPbI}_3(\text{p})$ is $2.25 \mu\text{m}$. It is not negligible that the traditional solution method cannot prepare PSC with such micrometer-thick perovskite/perovskite structures, so Yang et al. proposed a facile low-temperature solution-processing strategy combining the anti-solvent and dynamic dropping techniques to fabricate the micrometer-thick $\text{FAPbI}_3/\text{MAPbI}_3$. Eventually, the total thickness of the perovskite film reached about $2.65 \mu\text{m}$ [36].

Similar to above, varying the thickness of $\text{MAPbI}_3(\text{p})$ does not affect the strength of the BEF and the width of the SCR between $\text{MAPbI}_3(\text{p})$ and $\text{MAPbI}_3(\text{n})$, as shown in Fig. 19. From this it can be seen that the driving ability of the BEF for photogenerated carriers hardly changes. Besides, as

the thickness of $\text{MAPbI}_3(\text{p})$ increases, the transport of photogenerated carriers will be more hindered, and thus the FF will gradually decrease. Meanwhile, although increasing the thickness of $\text{MAPbI}_3(\text{p})$ absorbs more photons, it also increases the loss of photogenerated carriers, as shown in Fig. 20. Thus, the J_{SC} almost saturates when the thickness of $\text{MAPbI}_3(\text{p})$ increases to $2.05 \mu\text{m}$.

4. Conclusions

In this study, the perovskite layer was constructed in the form of a $\text{MAPbI}_3(\text{p})/\text{MAPbI}_3(\text{n})$ homojunction to reduce the carrier recombination rate in the PSCs. The BEF inside this homojunction can promote charge carrier separation and transport, and thus significantly suppressing carrier recombination. In addition, the effects of $\text{MAPbI}_3(\text{n})$ and $\text{MAPbI}_3(\text{p})$ doping concentration on the PV performance of PSCs were

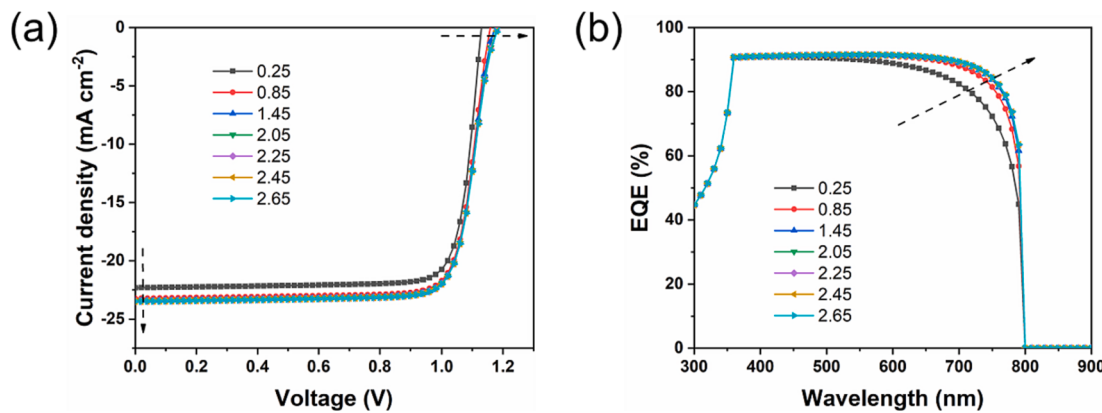


Fig. 18. (a) J-V curves, and (b) EQE curves of the PSCs corresponding to different thickness values of MAPbI₃(p).

Table 6

PV parameters of devices with different thickness values of MAPbI₃(p).

Thickness of MAPbI ₃ (p) (μm)	V _{OC} (V)	J _{SC} (mA/cm ²)	FF (%)	PCE (%)
0.25	1.13	22.31	82.40	20.77
0.85	1.16	23.23	80.76	21.73
1.45	1.17	23.43	79.87	21.94
2.05	1.18	23.48	79.26	21.99
2.25	1.18	23.48	79.13	22.00
2.45	1.19	23.48	79.02	22.00
2.65	1.19	23.49	78.94	22.00

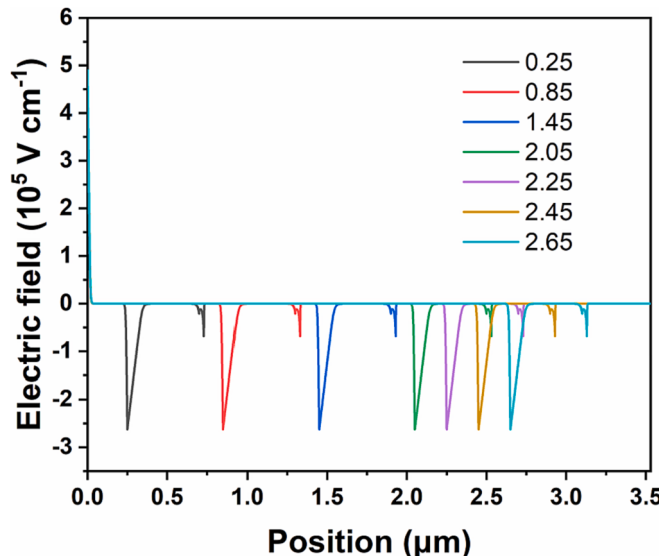


Fig. 19. Electric field of devices corresponding to different thickness values of MAPbI₃(p).

investigated separately. It was determined that when the N_D of MAPbI₃(n) was $1 \times 10^{17} \text{ cm}^{-3}$ and the N_A of MAPbI₃(p) was $1 \times 10^{18} \text{ cm}^{-3}$, the PCE of PSC reached 19.98 %. Besides, the impacts of MAPbI₃(n) and MAPbI₃(p) thickness on the PV performance were investigated. When the thickness of MAPbI₃(n) was 0.45 μm and that of MAPbI₃(p) was 2.25 μm, the PCE of PSC reached 22.00 %. The proposed MAPbI₃(p)/MAPbI₃(n) homojunction in the perovskite layer is a promising strategy to enhance the PCE of PSCs.

CRediT authorship contribution statement

Jiexiang Liang: . Yanan Wang: Investigation, Project

administration, Validation. Yufeng Zhang: Investigation, Resources, Supervision, Writing – review & editing. Xiaolin Liu: Investigation, Resources, Supervision, Writing – review & editing. Jia Lin: Conceptualization, Resources, Supervision, Writing – review & editing.

Declaration of competing interest

The authors declare that they have no known competing financial interests or personal relationships that could have appeared to influence the work reported in this paper.

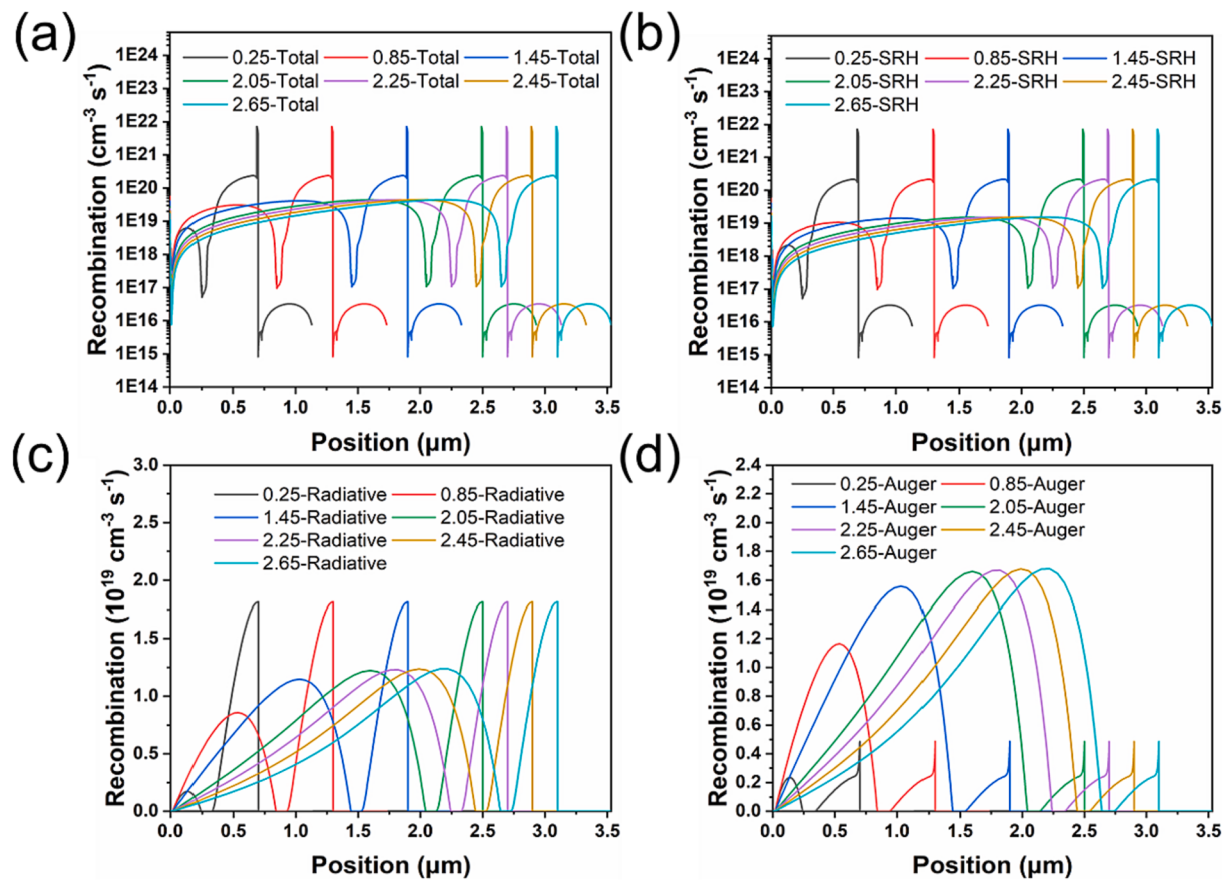


Fig. 20. (a) Total, (b) SRH, (c) radiative and (d) Auger recombination rates of devices corresponding to different thickness values of $\text{MAPbI}_3(\text{p})$.

Data availability

Data will be made available on request.

Acknowledgements

This work was supported by the National Natural Science Foundation of China (Grant Nos. 12174246, 62305204, 62305205), Science and Technology Commission of Shanghai Municipality (Grant No. 21010501300), and the Shuguang Program of Shanghai Education Development Foundation and Shanghai Municipal Education Commission (Grant No. 22SG51).

References

- [1] A. Kojima, K. Teshima, Y. Shirai, T. Miyasaka, Organometal halide perovskites as visible-light sensitizers for photovoltaic cells, *J. Am. Chem. Soc.* 131 (17) (2009) 6050–6051, <https://doi.org/10.1021/ja809598r>.
- [2] Best Research-Cell Efficiency Chart, (accessed: July 30, 2023). NREL, <https://www.nrel.gov/pv/cell-efficiency.html>.
- [3] Y. Shao, Z. Xiao, C. Bi, Y. Yuan, J. Huang, Origin and elimination of photocurrent hysteresis by fullerene passivation in $\text{CH}_3\text{NH}_3\text{PbI}_3$ planar heterojunction solar cells, *Nat. Commun.* 5 (2014) 5784, <https://doi.org/10.1038/ncomms6784>.
- [4] J. Xu, A. Buin, A.H. Ip, W. Li, O. Voznyy, R. Comin, M. Yuan, S. Jeon, Z. Ning, J. J. McDowell, P. Kanjanaboons, J.P. Sun, X. Lan, L.N. Quan, D.H. Kim, I.G. Hill, P. Maksymovych, E.H. Sargent, Perovskite-fullerene hybrid materials suppress hysteresis in planar diodes, *Nat. Commun.* 6 (2015) 7081, <https://doi.org/10.1038/ncomms8081>.
- [5] A. Abate, M. Saliba, D.J. Hollman, S.D. Stranks, K. Wojciechowski, R. Avolio, G. Grancini, A. Petrozza, H.J. Snaith, Supramolecular halogen bond passivation of organic-inorganic halide perovskite solar cells, *Nano Lett.* 14 (6) (2014) 3247–3254, <https://doi.org/10.1021/nl500627x>.
- [6] Y.-Z. Zheng, X.-T. Li, E.-F. Zhao, X.-D. Lv, F.-L. Meng, C. Peng, X.-S. Lai, M. Huang, G. Cao, X. Tao, J.-F. Chen, Hexamethylenetetramine-mediated growth of grain-boundary-passivation $\text{CH}_3\text{NH}_3\text{PbI}_3$ for highly reproducible and stable perovskite solar cells, *J. Power Sources* 377 (2018) 103–109, <https://doi.org/10.1016/j.jpowsour.2017.12.011>.
- [7] R. Wang, J. Xue, L. Meng, J.-W. Lee, Z. Zhao, P. Sun, L. Cai, T. Huang, Z. Wang, Z.-K. Wang, Y. Duan, J.L. Yang, S. Tan, Y. Yuan, Y. Huang, Y. Yang, Caffeine Improves the Performance and Thermal Stability of Perovskite Solar Cells, *Joule* 3 (6) (2019) 1464–1477, <https://doi.org/10.1016/j.joule.2019.04.005>.
- [8] W. Chen, Y. Wang, G. Pang, C.W. Koh, A.B. Djurišić, Y. Wu, B. Tu, Liu, F.Z., Chen, R., Woo, H.Y., Guo, X., He, Z., Conjugated Polymer-Assisted Grain Boundary Passivation for Efficient Inverted Planar Perovskite Solar Cells, *Adv. Funct. Mater.* 29 (27) (2019) 1808855, <https://doi.org/10.1002/adfm.201808855>.
- [9] X. Cao, L. Zhi, Y. Li, F. Fang, X. Cui, Y. Yao, L. Ci, K. Ding, J. Wei, Elucidating the Key Role of a Lewis Base Solvent in the Formation of Perovskite Films Fabricated from the Lewis Adduct Approach, *ACS Appl. Mater. Interfaces* 9 (38) (2017) 32868–32875, <https://doi.org/10.1021/acsmami.7b07216>.
- [10] X. Huang, G. Deng, S. Zhan, F. Cao, F. Cheng, J. Yin, J. Li, B. Wu, N. Zheng, Solvent Gaming Chemistry to Control the Quality of Halide Perovskite Thin Films for Photovoltaics, *ACS Cent. Sci.* 8 (7) (2022) 1008–1016, <https://doi.org/10.1021/acscentsci.2c00385>.
- [11] D.P. McMeekin, G. Sadoughi, W. Rehman, G.E. Eperon, M. Saliba, M.T. Horantner, A. Haghhighirad, N. Sakai, L. Korte, B. Rech, M.B. Johnston, L.M. Herz, H.J. Snaith, A mixed-cation lead mixed-halide perovskite absorber for tandem solar cells, *Science* 351 (6269) (2016) 151–155, <https://doi.org/10.1126/science.aad5845>.
- [12] M. Saliba, T. Matsui, J.Y. Seo, K. Domanski, J.P. Correa-Baena, M.K. Nazeeruddin, S.M. Zakeeruddin, W. Tress, A. Abate, A. Hagfeldt, M. Gratzel, Cesium-containing triple cation perovskite solar cells: improved stability, reproducibility and high efficiency, *Energy Environ. Sci.* 9 (6) (2016) 1989–1997, <https://doi.org/10.1039/C5EE03874J>.
- [13] E.H. Jung, N.J. Jeon, E.Y. Park, C.S. Moon, T.J. Shin, T.Y. Yang, J.H. Noh, J. Seo, Efficient, stable and scalable perovskite solar cells using poly(3-hexylthiophene), *Nature* 567 (7749) (2019) 511–515, <https://doi.org/10.1038/s41586-019-1036-3>.
- [14] N.J. Jeon, H. Na, E.H. Jung, T.-Y. Yang, Y.G. Lee, G. Kim, H.-W. Shin, S. Il Seok, J. Lee, J. Seo, A fluorene-terminated hole-transporting material for highly efficient and stable perovskite solar cells, *Nat. Energy* 3 (8) (2018) 682–689, <https://doi.org/10.1038/s41560-018-0200-6>.
- [15] Q. Jiang, Y. Zhao, X. Zhang, X. Yang, Y. Chen, Z. Chu, Q. Ye, X. Li, Z. Yin, J. You, Surface passivation of perovskite film for efficient solar cells, *Nat. Photon.* 13 (7) (2019) 460–466, <https://doi.org/10.1038/s41566-019-0398-2>.
- [16] H. Min, M. Kim, S.U. Lee, H. Kim, G. Kim, K. Choi, J.H. Lee, S.I. Seok, Efficient, stable solar cells by using inherent bandgap of alpha-phase formamidinium lead iodide, *Science* 366 (6466) (2019) 749–753, <https://doi.org/10.1126/science.aay7044>.

- [17] J. Cho, P.V. Kamat, How Chloride Suppresses Photoinduced Phase Segregation in Mixed Halide Perovskites, *Chem. Mater.* 32 (14) (2020) 6206–6212, <https://doi.org/10.1021/acs.chemmater.0c02100>.
- [18] B. Wang, J. Yang, L. Lu, W. Xiao, H. Wu, S. Xiong, J. Tang, C. Duan, Q. Bao, Interface Engineering of Air-Stable n-Doping Fullerene-Modified TiO_2 Electron Transport Layer for Highly Efficient and Stable Perovskite Solar Cells, *Adv. Mater. Interfaces* 7 (6) (2020) 1901964, <https://doi.org/10.1002/admi.201901964>.
- [19] J. Wang, J. Zhang, Y. Zhou, H. Liu, Q. Xue, X. Li, C.C. Chueh, H.L. Yip, Z. Zhu, A.K. Y. Jen, Highly efficient all-inorganic perovskite solar cells with suppressed non-radiative recombination by a Lewis base, *Nat. Commun.* 11 (2020) 177, <https://doi.org/10.1038/s41467-019-13909-5>.
- [20] W.S. Subhani, K. Wang, M. Du, X. Wang, S. Liu, Interface-Modification-Induced Gradient Energy Band for Highly Efficient CsPbIBr₂ Perovskite Solar Cells, *Adv. Energy Mater.* 9 (21) (2019) 1803785, <https://doi.org/10.1002/aenm.201803785>.
- [21] F. Wang, W. Geng, Y. Zhou, H.H. Fang, C.J. Tong, M.A. Loi, L.M. Liu, N. Zhao, Phenylalkylamine Passivation of Organolead Halide Perovskites Enabling High-Efficiency and Air-Stable Photovoltaic Cells, *Adv. Mater.* 28 (45) (2016) 9986–9992, <https://doi.org/10.1002/adma.201603062>.
- [22] Y. Wang, T. Zhang, M. Kan, Y. Li, T. Wang, Y. Zhao, Efficient $\alpha\text{-CsPbI}_3$ Photovoltaics with Surface Terminated Organic Cations, *Joule* 2 (10) (2018) 2065–2075, <https://doi.org/10.1016/j.joule.2018.06.013>.
- [23] Z. Wang, Q. Lin, F.P. Chmiel, N. Sakai, L.M. Herz, H.J. Snaith, Efficient ambient-air-stable solar cells with 2D–3D heterostructured butylammonium-caesium-formamidinium lead halide perovskites, *Nat. Energy* 2 (9) (2017) 17135, <https://doi.org/10.1038/nenergy.2017.135>.
- [24] P. Cui, D. Wei, J. Ji, H. Huang, E. Jia, S. Dou, T. Wang, W. Wang, M. Li, Planar p–n homojunction perovskite solar cells with efficiency exceeding 21.3%, *Nat. Energy* 4 (2) (2019) 150–159, <https://doi.org/10.1038/s41560-018-0324-8>.
- [25] Y.-N. Lu, J.-X. Zhong, Y. Yu, X. Chen, C.-Y. Yao, C. Zhang, M. Yang, W. Feng, Y. Jiang, Y. Tan, L. Gong, X. Wei, Y. Zhou, L. Wang, W.-Q. Wu, Constructing an n/n + homojunction in a monolithic perovskite film for boosting charge collection in inverted perovskite photovoltaics, *Energy Environ. Sci.* 14 (7) (2021) 4048–4058, <https://doi.org/10.1039/D1EE00918D>.
- [26] M. Burgelman, P. Nollet, S. Degraeve, Modelling polycrystalline semiconductor solar cells, *Thin Solid Films* 361–362 (2000) 527–532, [https://doi.org/10.1016/S0040-6090\(99\)00825-1](https://doi.org/10.1016/S0040-6090(99)00825-1).
- [27] K.D. Jayan, Complete modelling and simulation of all perovskite tandem solar cells, *Materials Science and Engineering: B* 294 (2023), <https://doi.org/10.1016/j.mseb.2023.116506>.
- [28] G. Pindolia, S.M. Shinde, Potassium tin mixed iodide-bromide KSn(I_{1-x}Bx)₃ [x = 0.25,0.5,0.75,1] perovskites for solar cell absorbers: A computational study, *Materials Science and Engineering: B* 297 (2023), <https://doi.org/10.1016/j.mseb.2023.116795>.
- [29] V. Deswal, S. Kaushik, R. Kundara, S. Baghel, Numerical simulation of highly efficient Cs₂AgInBr₆-based double perovskite solar cell using SCAPS 1-D, *Materials Science and Engineering: B* 299 (2024), <https://doi.org/10.1016/j.mseb.2023.117041>.
- [30] M.M. Ivashchenko, O.V. Diachenko, A.S. Opanasyuk, I.P. Buryk, D.V. Kuzmin, A. Čerškus, O. Šopovalov, S.V. Plotnikov, I.A. Gryshko, A numerical simulation of solar cells based on the CuO and Cu₂O absorber layers with ZnMgO window layer, *Materials Science and Engineering: B* 300 (2024), <https://doi.org/10.1016/j.mseb.2023.117133>.
- [31] J.M. Richter, M. Abdi-Jalebi, A. Sadhanala, M. Tabachnyk, J.P.H. Rivett, L. M. Pazos-Outon, K.C. Godel, M. Price, F. Deschler, R.H. Friend, Enhancing photoluminescence yields in lead halide perovskites by photon recycling and light out-coupling, *Nat Commun* 7 (2016) 13941, <https://doi.org/10.1038/ncomms13941>.
- [32] S. Mushtaq, S. Tahir, A. Ashfaq, R. Sebastian Bonilla, M. Haneef, R. Saeed, W. Ahmad, N. Amin, Performance optimization of lead-free MASnBr_3 based perovskite solar cells by SCAPS-1D device simulation, *Sol. Energy* 249 (2023) 401–413, <https://doi.org/10.1016/j.solener.2022.11.050>.
- [33] H. Abedini-Ahangarkola, S. Soleimani-Amiri, S. Gholami Rudi, Modeling and numerical simulation of high efficiency perovskite solar cell with three active layers, *Sol. Energy* 236 (2022) 724–732, <https://doi.org/10.1016/j.solener.2022.03.055>.
- [34] Y. Sun, W. Chen, Z. Sun, A mini review: Constructing perovskite p-n homojunction solar cells, *Chinese Chem. Lett.* 33 (4) (2022) 1772–1778, <https://doi.org/10.1016/j.ccl.2021.08.055>.
- [35] L. Lin, L. Jiang, P. Li, H. Xiong, Z. Kang, B. Fan, Y. Qiu, Simulated development and optimized performance of CsPbI₃ based all-inorganic perovskite solar cells, *Solar Energy* 198 (2020) 454–460, <https://doi.org/10.1016/j.solener.2020.01.081>.
- [36] X. Yang, Q. Li, Y. Zheng, D. Luo, Y. Zhang, Y. Tu, L. Zhao, Y. Wang, F. Xu, Q. Gong, R. Zhu, Perovskite hetero-bilayer for efficient charge-transport-layer-free solar cells, *Joule* 6 (6) (2022) 1277–1289, <https://doi.org/10.1016/j.joule.2022.04.012>.